Supplementary Materials for

Surface Plasmon Driven Atomic Migration Mediated by Molecular Monolayer

Qihong Hu[1], Jieyi Zhang[1], Ramya Emusani[1], Junchao Yang[1], Xin Zuo[1], Yiran Wang[1], Yonggang Huang [2,*] Dong Xiang[1,*]

This PDF file includes:

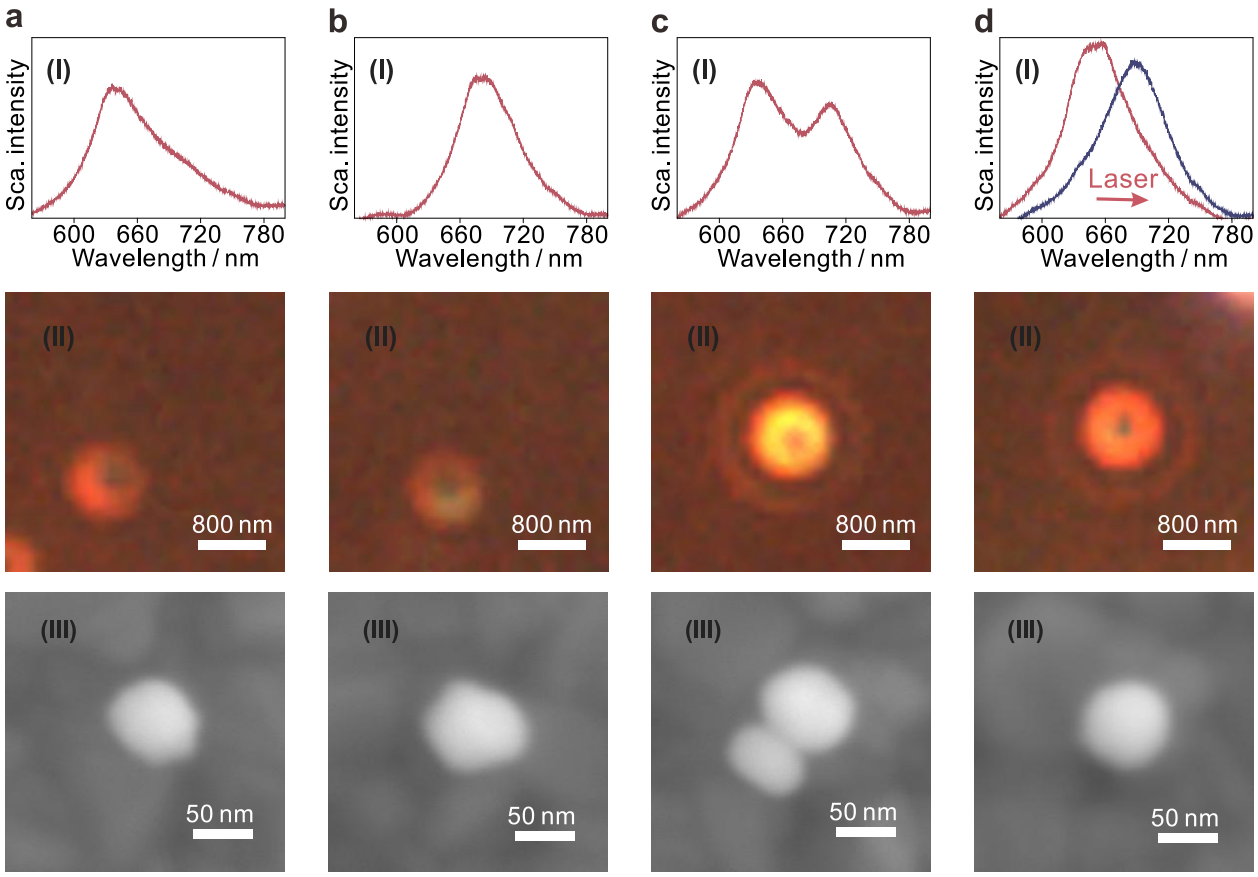

Fig. S1 DF scattering spectra (I), DF images (II), and SEM images (III) of various NPoMs. **a** Most nanoparticles with ~ 60 nm diameter exhibit a resonance wavelength around ~ 640 nm. **b** Larger nanoparticles exhibit longer resonance wavelengths around ~ 680 nm. **c** The DF image appears as a single point but actually represents two nanoparticle clusters, evidenced by two distinct resonance peaks in the scattering spectrum and confirmed by the SEM image. **d** The laser-irradiated NPoM showing redshift exhibits no significant morphological changes in the SEM image.

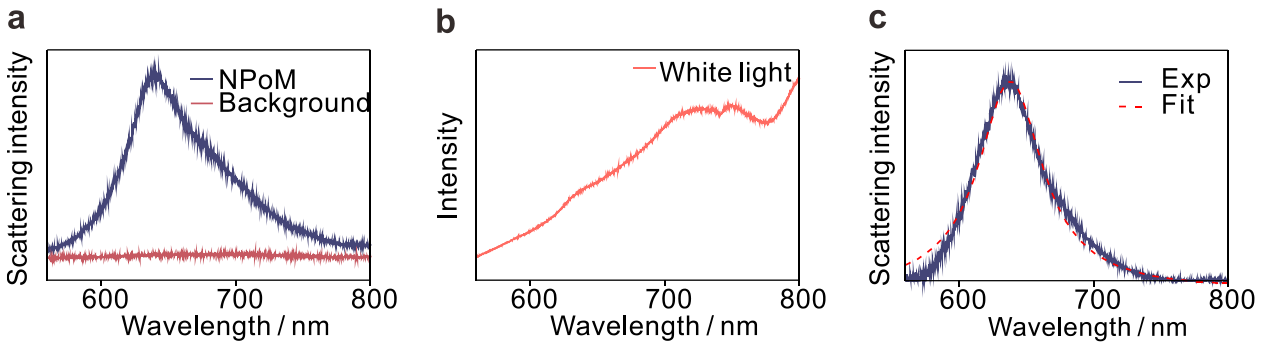

Fig. S2 Data processing and fitting of scattering spectra to extract resonance wavelengths. **a** Scattering spectra of NPoM and the blank background signal without NPoM. **b** Intensity distribution of the white light source for the DF scattering spectra measurements and DF imaging. **c** Scattering spectra of a NPoM with its Lorentzian fitting curve.

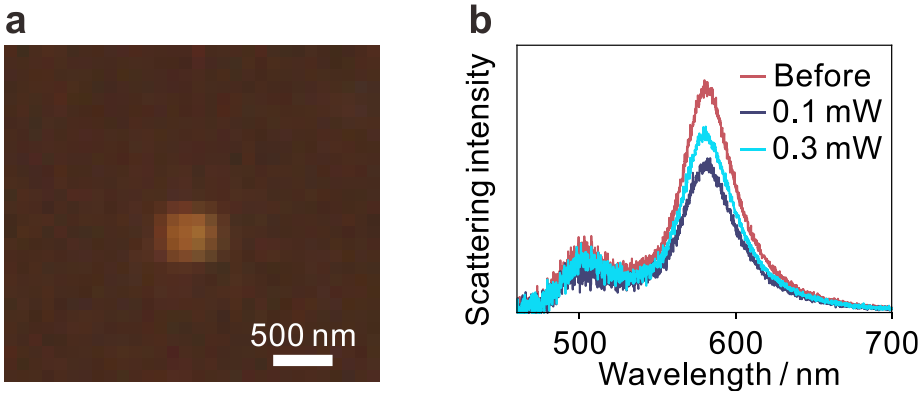

Fig. S3 Nanoparticles on a bare glass substrate without a self-assembled monolayer. **a** DF image of the NP on glass. **b** DF scattering spectra recorded before laser irradiation, after 0.1 mW laser irradiation for 30 seconds, and after 0.3 mW laser irradiation for 30 seconds.

To evaluate the photothermal response of the gold nanoelectrode system under laser illumination, we conducted coupled simulations using COMSOL Multiphysics. The modelling process consisted of two sequential steps: (1) electromagnetic field simulation to obtain the spatial distribution of the electric field E and the heat power density Q_d; and (2) heat transfer simulation to determine the steady-state temperature distribution [*S1*]. The electromagnetic field calculations are described in Supplementary Note S1. The heat power density Q_d was computed using the following relation: $Q_d = \omega\varepsilon_0 \mathrm{Im}(\varepsilon_r)|\boldsymbol{E}|^2/2$, where ε_r is the relative dielectric constant. Here, we adopt the value for silver at 645 nm: $\varepsilon_r = -11.304 - 0.78197i$. In the second step, the spatial distribution of Q_d was used as the heat source input in the "Heat Transfer in Solids" module. The thermal conductivities of gold and surrounding materials were taken from standard literature values. The ambient temperature at the outer layer of the PML was fixed at $T_0 = 293$ K. Under steady-state conditions, the temperature distribution T was obtained by solving the heat diffusion equation: $\nabla\cdot[-\kappa\nabla T] + Q_d = 0$. The maximum temperature increases, defined as $\Delta T = T - T_0$, were found to be approximately 0.9 K and 2.8 K for incident laser powers of 0.1 mW and 0.5 mW, respectively (Fig. S4). These results indicate that the photothermal effect in our system is minimal, confirming that the observed atomic migration cannot be attributed to thermally induced melting.

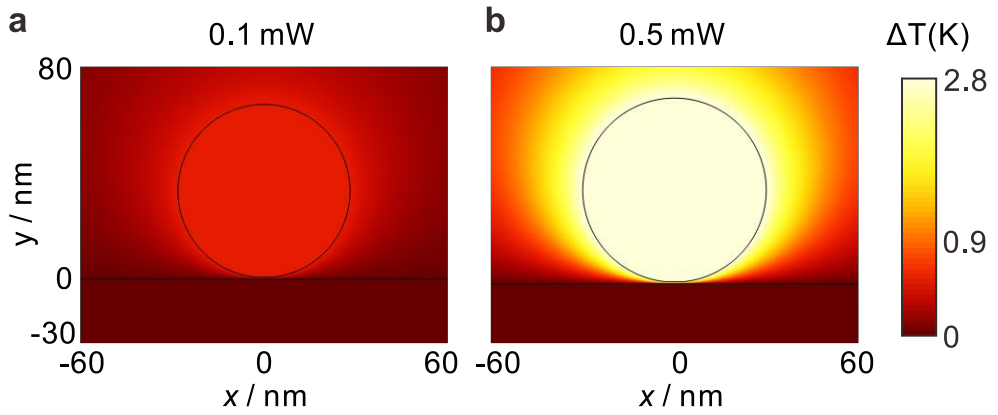

Fig. S4 Distribution of temperature increase near the NPoM structure under laser irradiation with an irradiation power of **a)** 0.1 mW and **b)** 0.5 mW.

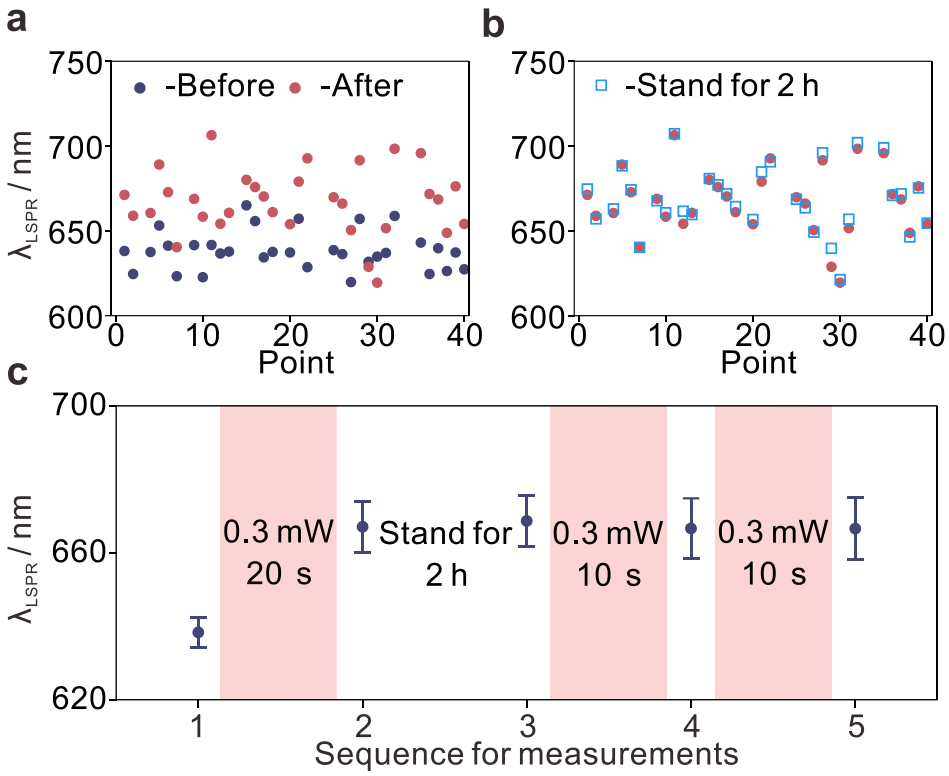

Fig. S5 Effect of continuous irradiation and static storage in dark on the resonance wavelength. **a** Resonance wavelength of each NPoM before and after laser irradiation (0.3 mW, 10 s). In total, 40 NPoMs were measured. **b** Resonance wavelength measured after 2 h of static storage in dark compared to the initial resonance wavelength before second-round laser irradiation. **c** Resonance wavelength at different stages: initial stage before irradiation, after laser irradiation, after 2 h of static storage in dark, and after two additional 10 s laser irradiations. The resonance shifting is observed only after the initial 20 s laser irradiation. Only results with coefficient of determination $R^2 > 0.92$ were considered. The coefficient of determination R^2 is defined as $R^2 = 1 - SS_{res} / SS_{tot}$, where SS_{res} is the residual sum of squares and SS_{tot} is the total sum of squares.

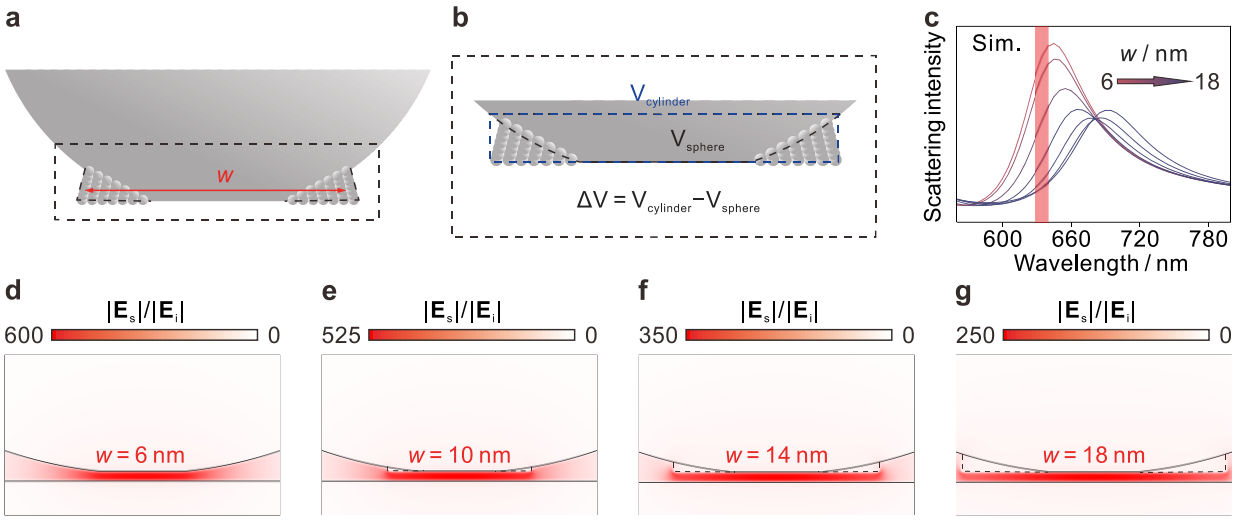

Fig. S6 The number of atoms required to increase *w* and, as well as the theoretically calculated scattering intensity and EF with different *w*. **a** Schematic diagram of the increase in *w* due to atomic migration. **b** The model for the calculation of *w*, which can be used to calculate the number of migrated atoms required to achieve the target resonance wavelength. **c** Theoretically calculated scattering intensity when *w* increases from 6 nm to 18 nm. The resonance peak red shifts as *w* increases from 6 nm to 10 nm. The rectangle indicates the wavelength of incident laser (640 nm). **d-g** Enhancement factors when *w* is 6 nm, 10 nm, 14 nm, and 18 nm upon the laser irradiation.

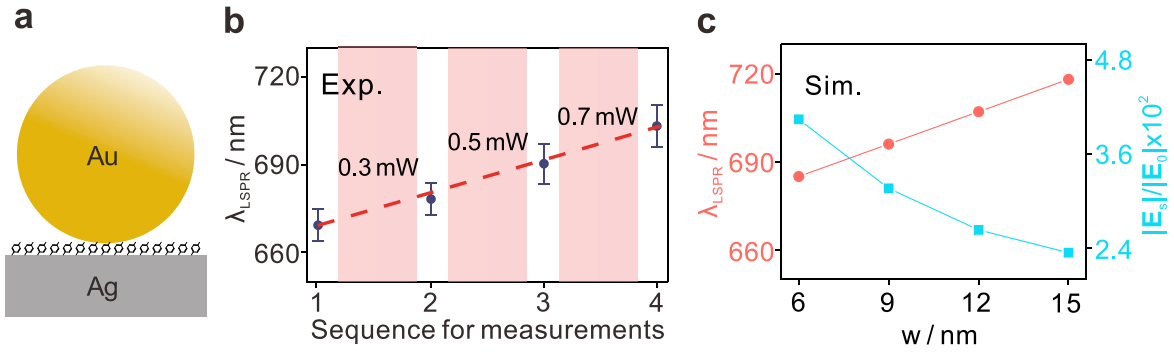

Fig. S7 Gradually increasing laser power resulting in a further redshift of the resonance wavelength. a Schematic diagram of the NPoM structure with Au nanoparticle on Ag substrate bridged by **a** SAM. **b** Resonance wavelength shifts under 30 s laser irradiation with a power of 0.3 mW, 0.5 mW, and 0.7 mW in sequence. **c** Simulations indicate that redshift and EF reductions can be caused by an increased cross-section (*w*) at the nanoparticle bottom.

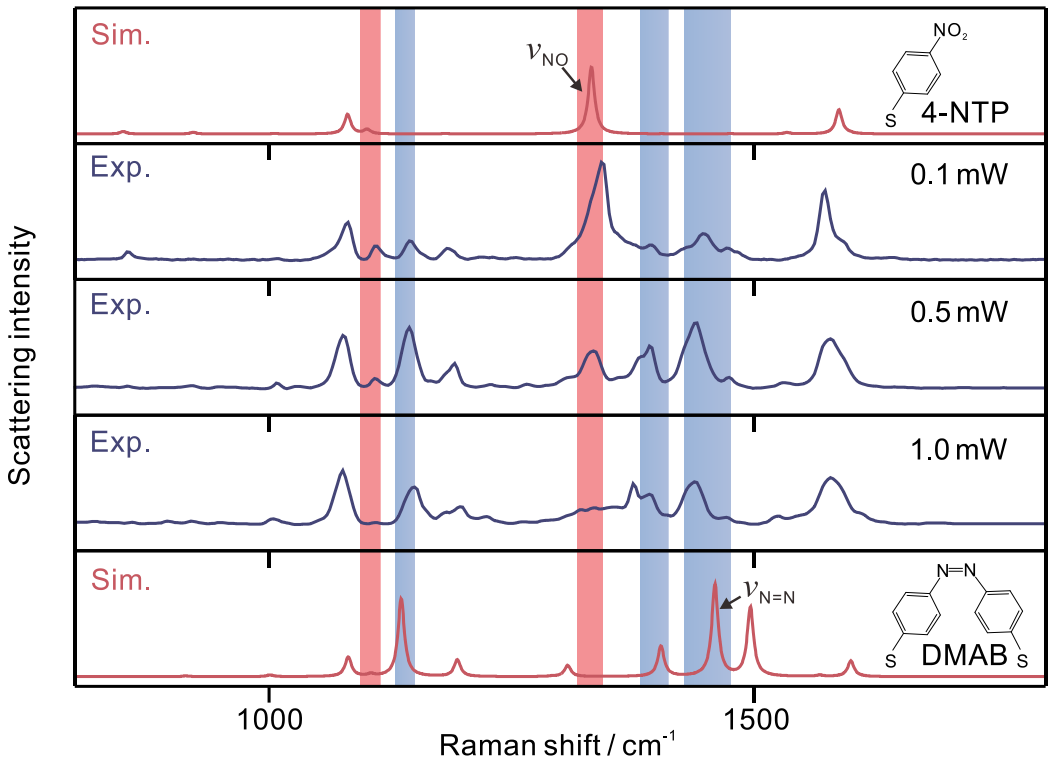

Fig. S8 The Raman spectra of 4-NTP and DMAB calculated using Gaussian 09, as well as the experimental Raman spectra of a NPoM irradiated with different laser powers for 30 seconds. Upon a high-power laser irradiation, the intensity of vibration modes (-NO_2) decreases as marked by the red rectangle, indicating that more 4-NTP is transformed to other kinds of molecules without -NO_2 group anymore. In contrast, the intensity of vibration modes (N=N) increases as marked by the blue rectangular, indicating that more was generated upon high-power laser irradiation. The *in-situ* measurement of Raman spectra confirmed that the SPP will induce a chemical reaction which transforms 4-NTP to DMAB.

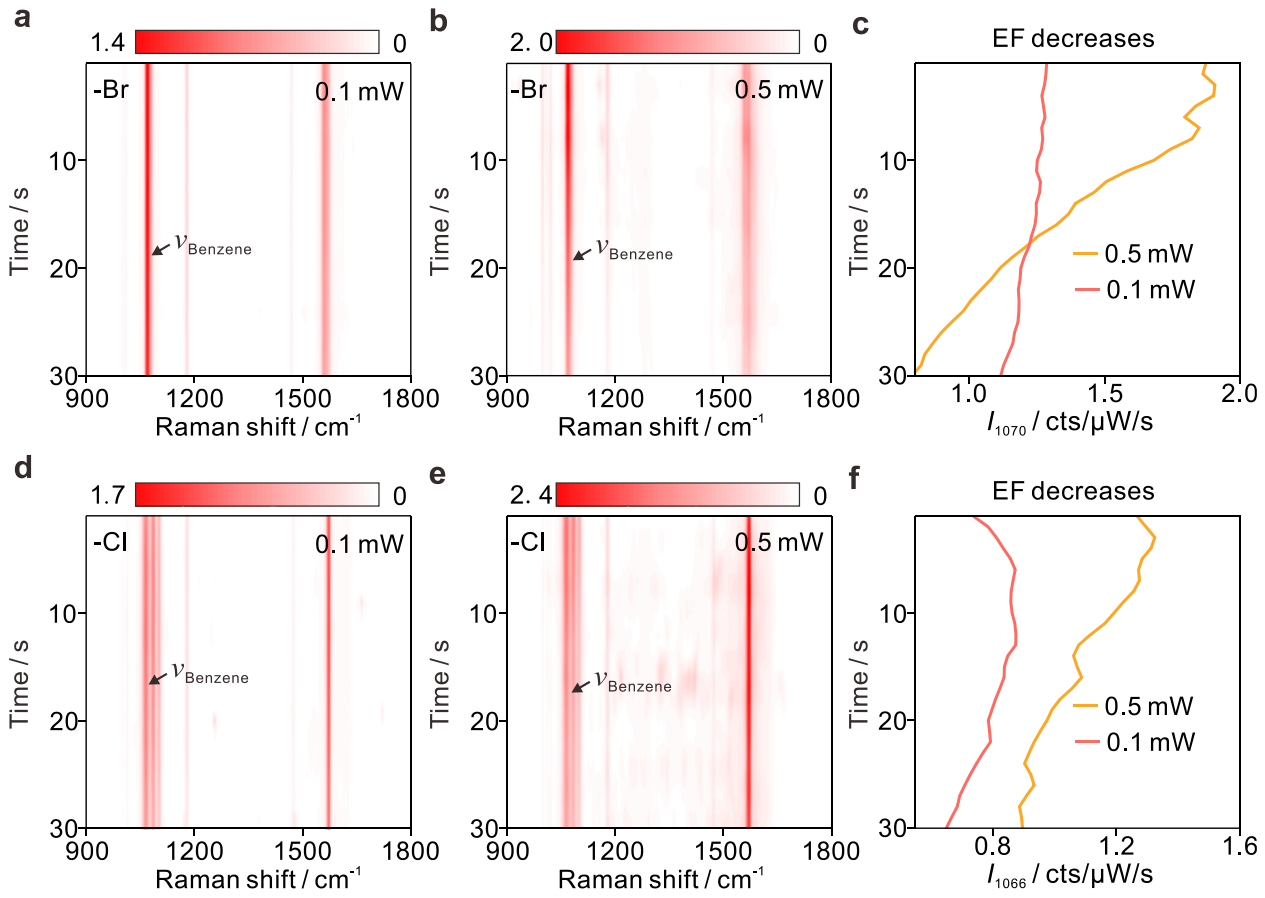

Fig. S9 Raman spectra evolution of NPoM with sandwiched 4-BTP and 4-CTP SAMs. Raman spectra of 4-BTP measured under laser irradiation with a power of **a** 0.1 mW and **b** 0.5 mW. d Raman spectra of 4-CTP measured under **d** 0.1 mW and **e** 0.5 mW laser irradiation. **c** Intensity of I_{1070} during laser irradiation for 4-BTP. **f** Intensity of I_{1066} for 4-CTP during laser irradiation. Unit for color bar: cts/μW/s.

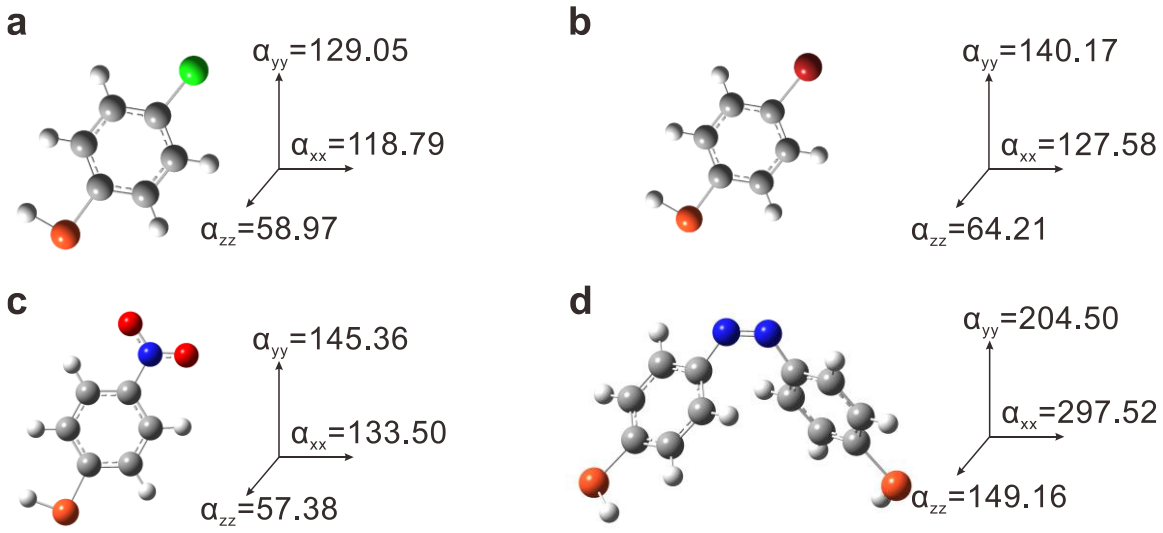

Fig. S10 Static polarizabilities (atomic units) along three directions calculated using Gaussian 09 package. The calculations employed the hybrid exchange-correlation functional B3LYP and the 6-311+G (d,p) basis set. Molecules analyzed include: **a** 4-CTP, **b** 4-BTP, **c** 4-NTP and **d** DMAB. The DMAB, transformed from two 4-NTP molecules, has the largest polarizability along the vertical direction (perpendicular to the substrate surface).

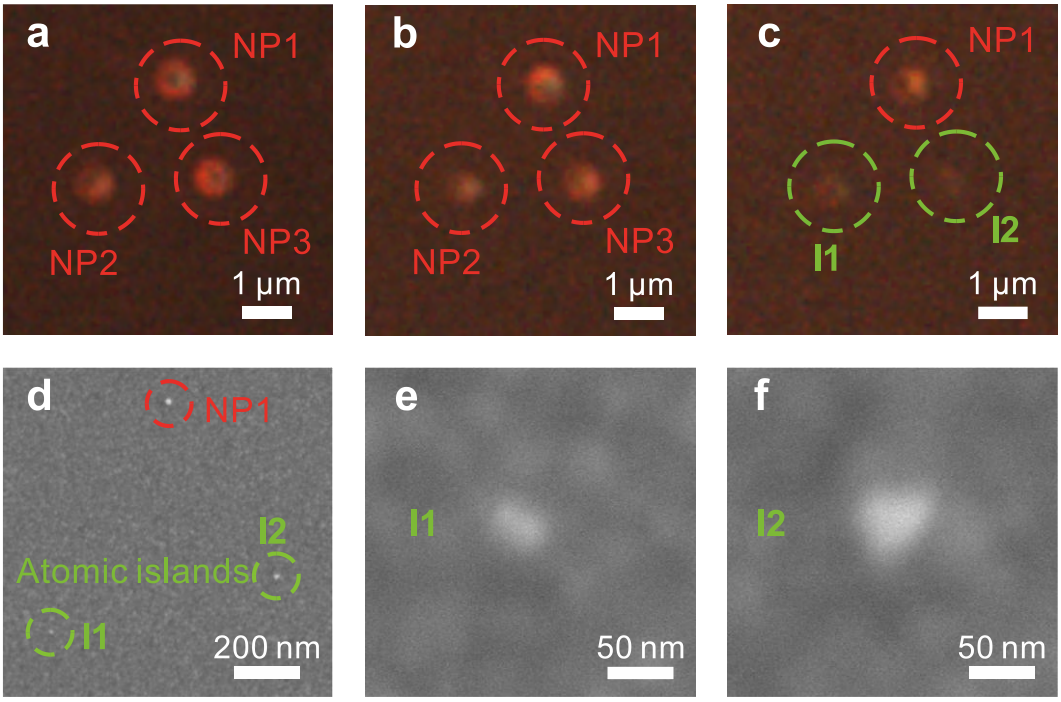

Fig. S11 Preliminary experiments in fabricating atomic-scale metal island arrays. **a** DF imaging of three Ag on Au NPoMs before laser irradiation. **b** DF image of three Ag on Au NPoMs after laser irradiation. **c** DF image of the NPoM after rinsing with ethanol. It shows that two nanoparticles were removed, while part of migrated atomic islands were retained. **d** SEM image of the sample as shown in Fig. c, in which two residual metal atomic islands can be observed after the removal of nanoparticle, confirming that metal atoms migrated to the top of SAM during the laser irradiation. **e** and **f** Zoomed SEM images of the atomic islands as presented in **d**.

Although the redshift in LSPR and the DF imaging strongly suggest the atomic migration, they are ultimately indirect evidence. Higher-resolution structural characterization (*e.g.*, HRTEM) directly supports the claim. To the best of our knowledge, it while faces technical challenges. First, TEM requires transparent substrates with respect to electron beam, which is fundamentally incompatible with the metallic mirror configuration used in NPoM structures. Second, the ultrahigh vacuum conditions required for HRTEM could potentially damage or remove the atomic islands, which are weakly adsorbed on the molecular layer. This characterization limitation needs to be broken.

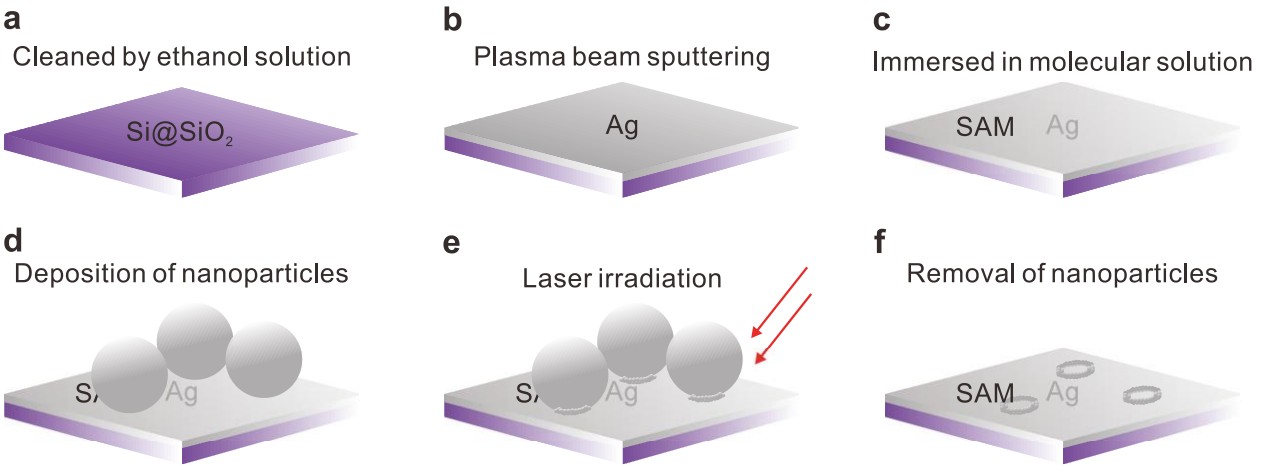

Fig. S12 Schematic diagram of the principle for constructing atomic-island arrays by molecule-assisted atomic migration. **a** Cleaning a Si substrate (with a SiO_2 layer) by rinsing it with ethanol and deionized water, then drying it with nitrogen. **b** Depositing a ~200 nm metal film onto the substrate by ion sputtering. **c** Immersing the metal-coated substrate in an ethanolic solution of the target thiol-terminated molecules for 12 h to form SAM, followed by rinsing off excess molecules with ethanol and drying it with nitrogen. **d** Drop-casting the nanoparticle colloid onto the SAM and rinsing it with distilled water, then drying it under nitrogen to build the nanoparticle-on-mirror (NPoM) structure. **e** Irradiating the NPoM with laser light. Molecule-assisted atomic migration Once an atom is pulled out from the metal surface, lateral diffusion enables it to move to the surrounding space around the bottom of the nanoparticle. The atomic migration may result in a symmetric atomic island around the bottom center of the nanoparticle. **f** Rinsing the sample with ethanol and water to remove the nanoparticles, revealing arrays of atomic islands at their former positions.

Supplementary Note S1. Numerical simulation based on COMSOL

The scattering cross section and EF of the NPoM structure were calculated using the Radio Frequency (RF) Module in COMSOL Multiphysics. To leverage the rotational invariance of the NPoM structure, the model was simplified into a 2.5D configuration, which significantly reduced computational resource requirements. The metal film was modeled with a thickness of 100 nm, while the nanoparticle was approximated as a sphere with a small cross-section at its bottom surface. Define that there is a facet w at the bottom of the nanoparticle. To accurately simulate the nanoscale gaps in NPoM, quantum effects were incorporated into the model. Specifically, quantum hydrodynamic theory (QHT) was employed to account for non-local quantum pressure effects, electron spill-out, and Landau damping, ensuring a comprehensive representation of the system behavior. The linearized QHT response is governed by the following equations in the frequency domain [*S2-S4*]:

$$\nabla\times\nabla\times\mathbf{E_s}-\frac{\omega^2}{c^2}\varepsilon_{bg}\mathbf{E_s}-\omega^2\mu_0\mathbf{P}-\frac{\omega^2}{c^2}\varepsilon'_\infty(\omega)(\mathbf{E_i}+\mathbf{E_s})=0, \tag{1}$$

$$\frac{en_0}{m_e}\nabla\left(\frac{\delta G[n]}{\delta n}\right)_1-\frac{e}{m_e}\nabla\cdot(\eta_\sigma\boldsymbol{\sigma})+(\omega^2+i\gamma\omega)\mathbf{P}=-\varepsilon_0\omega_p^2(\mathbf{E_s}+\mathbf{E_i}). \tag{2}$$

Here $\mathbf{E_i}$ ($\mathbf{E_s}$) and $\mathbf{P}$ are the incident (scattered) electric field and the polarization vector, respectively. c, ε_0 and μ_0 are the speed of light, the permittivity, and the permeability in a vacuum, respectively. m_e and e are the electron mass and charge. γ represents the phenomenological damping rate, $\omega_p=\sqrt{e^2n_0/m_e\varepsilon_0}$ is the plasma frequency with n_0 being the ground state electron density. ε_{bg} is the permittivity of the background dielectric medium, $\varepsilon'_\infty(\omega)$ contains the bound electron response in the noble metal,

$$\varepsilon'_\infty(\omega)=\varepsilon_\infty-\frac{\omega_{p,2}^2}{\omega^2-\omega_{0,2}^2+i\omega\gamma_2}-\varepsilon_{bg}. \tag{3}$$

Where the parameters of gold and silver here adopt the values from the literature [*S3*], n_0 is the ground state electron density. We obtain n_0 in a self-consistent way, which has the advantage that it can be used to calculate nanostructures of arbitrary geometry. The equation reads,

$$\nabla \cdot \varepsilon(\mathbf{r}) \nabla \left(\frac{\delta G[n]}{\delta n} \right)_{n=n_0} + e^2 \left(n_0 - n^+ \right) = 0, \tag{4}$$

with $n^+ = \left(4\pi r_s^3/3\right)^{-1}$ being the positive charge density for the uniform jellium background. In this work, we focus on Au with Wigner-Seitz radius $r_s = 3.12a_0$ and $r_s = 3.05a_0$ for Ag. a_0 is the Bohr radius. $G[n] = T_{TF}[n] + \lambda_{vW} T_{vW}[n] + E_{XC}[n]$ are the Thomas-Fermi, von Weizsäcker kinetic energy functionals and exchange-correlation energy functional, respectively. λ_{vW} is not well defined and usually in the range from 1/9 to 1. $\boldsymbol{\sigma}$ is a viscoelastic tensor used to describe Landau damping, η_σ is the intensity parameter of Landau damping. We selected the energy functional form and parameters from the literature, which were calibrated using time-dependent density functional theory [*S4*]. Where $\lambda_{vW} = 0.43$ for stationary-state calculation, $\lambda_{vW} = 0.70$ for optical-response calculation, and $\eta_\sigma = 7$. Interestingly, by disregarding the quantum effect-related terms in Eq. 2 and defining $n_0 = n^+$, QHT simplifies to the Lorentz-Drude model,

$$\left(\omega^2 + i\gamma\omega\right)\mathbf{P} = -\varepsilon_0 \omega_p^2 \left(\mathbf{E_s} + \mathbf{E_i}\right). \tag{5}$$

Despite simplifying the model to a 2.5D configuration, calculating structures spanning hundreds of nanometers using QHT remains computationally intensive. To address this challenge, further approximations were implemented. Specifically, QHT calculations were restricted to the 5 nm regions on the surfaces of nanoparticles and metal films, while the remaining regions of the metal films were modeled using the local response approximation. This hybrid approach effectively captures critical quantum effects within the nano-gap and ensures accurate simulation of nanoparticle surface phenomena while substantially reducing computational demands. In the grid configuration, the 0.5 nm regions on the surfaces of nanoparticles and metal films, where significant

variations in ground state density occur, required a fine grid size of 0.03 nm. For the metal interior, a coarser grid size of 1 nm was sufficient, whereas the air region was modeled with a 20 nm grid. To accurately resolve the nano-gap, a mapping grid with 20 layers was employed. Additionally, the surrounding area was enclosed by a perfect matching layer to simulate an infinite region, with the metal film embedded within this layer to replicate an infinite metallic surface.

Figure S13 presents the results of calculations using the QHT and the local response approximation model. In the classical model, the resonance wavelength continuously redshifts as the gap decreases, with larger values of w corresponding to longer resonance wavelengths (Fig. S13e). However, QHT calculations, which incorporate the electron spill-out effect, reveal that the resonance wavelength begins to blueshift when the gap narrows to approximately 0.6 nm (Fig. S13b). This finding suggests that attributing the experimental redshift of the resonance wavelength solely to gap variation is not justified. For the full width at half maximum (FWHM, Figs. S13c and f), QHT calculations indicate that the FWHM increases with both decreasing gap size and increasing *w*/D. Conversely, the classical model shows minimal changes in the FWHM, highlighting the distinct predictions made by the two approaches.

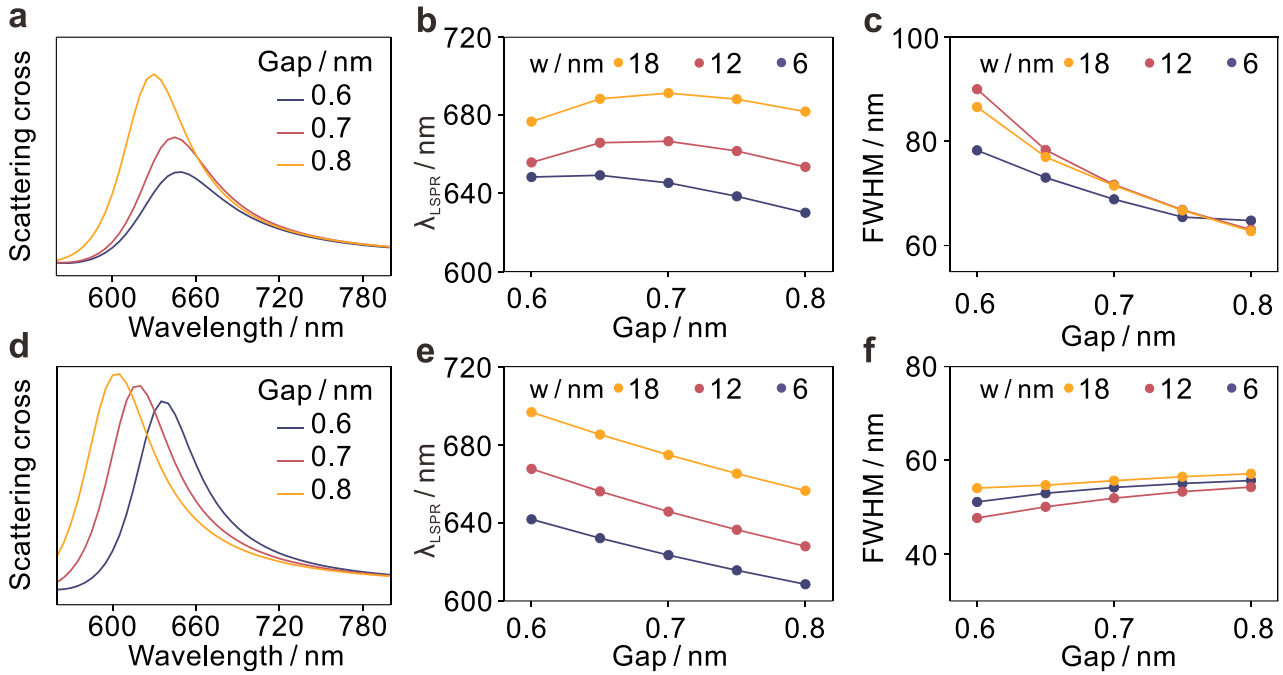

Fig. S13 Scattering cross sections, LSPR wavelengths, and FWHM calculated using different simulation methods. **a-c**: Results obtained from QHT. **d-f:** Results obtained from the local response approximation model. Detailed information for the method introduction can be found in Supplementary Note S1.

Supplementary Note S2. Dipole-dipole force estimation

The dipole – dipole interaction energy between a metal atom and its nearest molecular tip can be denoted as

$$U(r)=\frac{1}{4\pi\varepsilon_0 r^3}\left[\mathbf{p}_{\mathrm{M}}\cdot\mathbf{p}_{\mathrm{t}}-3\left(\mathbf{p}_{\mathrm{M}}\cdot\mathbf{r}\right)\cdot\left(\mathbf{p}_{\mathrm{t}}\cdot\mathbf{r}\right)\right]. \tag{6}$$

Here, $r = a+z$ is the dipole – dipole distance, a is the radius of the metal atom, and z is the distance from the molecular tip to the metal edge. Assuming the metal atom is positioned directly above the molecular tip (i.e., $\mathbf{p}\cdot\mathbf{r} = pz$), Eq. 6 simplifies to

$$U=\frac{-p_M p_t}{2\pi\varepsilon_0 r^3}. \tag{7}$$

By substituting the effective polarizability (α_{eff}) of the molecular tip into Eq. 7 [*S5*], we obtain

$$U=\frac{-p_M}{2\pi\varepsilon_0 r^3}\left(\alpha_t\varepsilon_0\mathbf{E}_{\mathrm{dip}}+\alpha_t'\varepsilon_0\nabla\mathbf{E}_{\mathrm{dip}}\right)\zeta. \tag{8}$$

Where $\mathbf{E}_{\mathrm{dip}}$ denotes the electric field generated by the metal atom, with its z-component represented as

$$\mathbf{E}_{\mathrm{dip}}\left(\mathbf{r}\right)=\mathbf{E}_{\mathrm{s}}+\frac{1}{4\pi\varepsilon_0}\left(\frac{2p_{\mathrm{M}}}{r^3}\right). \tag{9}$$

Eq. 9 derived from the paper [*S6*], describes the light field of metal atoms in the corona cavity and agrees with the results of time-dependent density functional theory. Defining $p_{\mathrm{M}} = 4\pi\varepsilon_0 a^3\mathbf{E}_{\mathrm{s}}$ and substituting it along with Eq. 9 into Eq. 8—while neglecting the $\nabla\mathbf{E}_{\mathrm{dip}}$—yields

$$U=-2\varepsilon_0\mathbf{E}_{\mathrm{s}}{}^2\frac{a^3}{r^3}\left(\alpha_t\left(1+\frac{2a^3}{r^3}\right)\right)\zeta. \tag{10}$$

Using the substitution r = z + a and incorporating the effective polarizability correction factor into Equation [*S5*] gives

$$U=-2\varepsilon_0\mathbf{E}_{\mathrm{s}}{}^2\frac{1}{\left(1+z/a\right)^3}\left(\alpha_t\left(1+\frac{2}{\left(1+z/a\right)^3}\right)\right)\frac{1}{1-\left(\kappa/z\right)^3}. \tag{11}$$

When the molecular tip and the metal atom are in close proximity, a relationship is observed as

$$U \sim -2\varepsilon_0 \mathbf{E}_s^{\,2} \left(3\alpha_t\right) \frac{1}{1-\left(\kappa/z\right)^3}. \tag{12}$$

Defining $U \sim -\varepsilon_0 \mathbf{E}_s^{\,2} a^3 \varsigma\zeta$ accordingly, the force generated by the metal atom being extracted is

$$F \sim -\varepsilon_0 \mathbf{E}_s^{\,2} a^2 \varsigma\zeta \sim F_o \varsigma\zeta. \tag{13}$$

Compared with the traditional optical force F_0, two additional terms appear: one is the correction factor for the actual polarizability of the molecular tip ζ, and the other is related to the dipole moment of the molecular tip $\varsigma = 6\alpha_t / a^3$ [*S5*]. Finally, by employing the traditional gradient force calculated *via* the finite element method, the dipole – dipole interaction force can be estimated.

Supplementary Note S3. Spatially controlling of atomic-island arrays

Here, we propose two promising strategies for the spatial control of atomic islands, as shown in Fig. S14. The first strategy is molecular pattern-guided nanoparticle deposition, as shown in Fig. S14a. First, a SAM pattern can be defined at the target locations using electron-beam lithography (EBL). Molecules are only adsorbed on the metal surface *via* the anchoring group, and nanoparticles can then be tethered strongly on the functionalized molecular layer, thereby the molecular pattern layer can guide the subsequent deposition of nanoparticles. Upon laser illumination, atomic islands are preferentially generated around the base of the nanoparticle.

The second proposed strategy is laser spot scanning-guided atomic migration, as shown in Figs. S14b. First, we deposited a layer of high-density nanoparticles on a metal substrate covered with a SAM. Second, a laser beam can be used to selectively irradiate specific locations, *e.g.*, using direct laser writing equipment to irradiate a few nanoparticles located at the target position. The irradiation resolution was mainly determined by the density of nanoparticles and the size of the laser spot. Only the nanoparticles in these illuminated regions undergo atomic migration, allowing for the fabrication of island arrays.

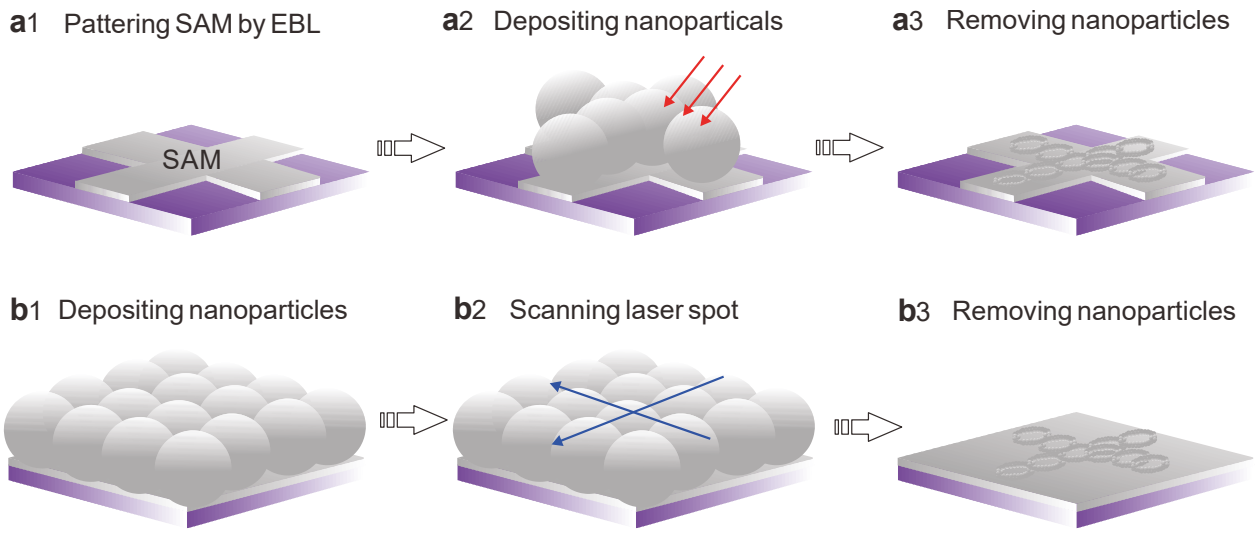

Fig. S14 Schematic diagram of two strategies for spatially controlling atomic-islands array. **a**1 Self-assembling molecules on the patterned metal surface which is pre-fabricated by EBL. **a**2 Depositing nanoparticles onto the patterned SAM surface. The nanoparticles selectively adsorb on the functionalized SAM surface. **a**3 Atomic islands obtained around the base of the nanoparticle after removing the nanoparticle. **b**1 Deposition of a high density of nanoparticles across the whole metal surface above the SAM. **b**2 Scanning the sample with a focused laser beam to selectively irradiate targeted regions, inducing localized atomic migration. **b**3 Removing the nanoparticles with ethanol and water to reveal spatially controlled atomic-island arrays at the laser-illuminated regime.

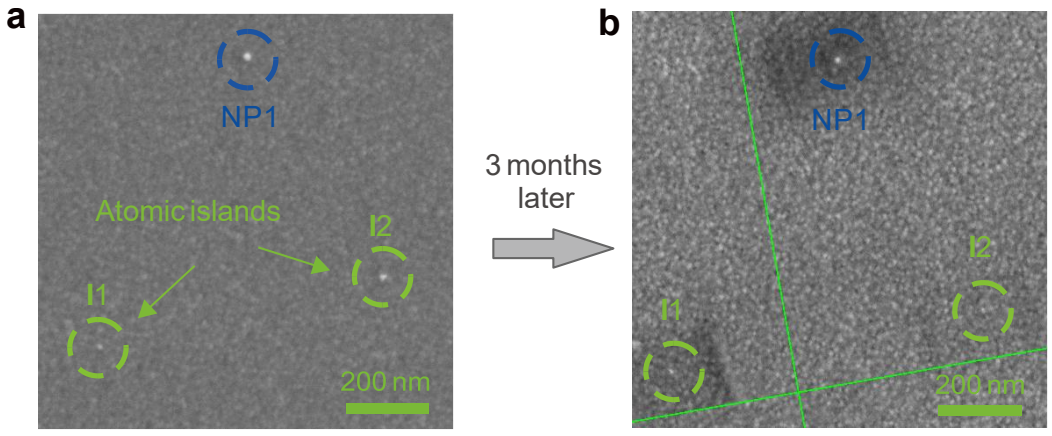

Fig. S15 SEM image of the samples before and after 3 months storage. **a** The SEM of the fresh sample after light irradiation and removing of the nanoparticle. **b** The SEM of the sample the same as **a** after being stored for three months.

References

S1. Zhan C, Wang G, Yi J, Wei J-Y, Li Z-H, Chen Z-B, et al. Single-Molecule Plasmonic Optical Trapping. Matter. 2020;3(4):1350-60.

S2. Ciracì C. Current-dependent potential for nonlocal absorption in quantum hydrodynamic theory. Phys Rev B. 2017;95(24):245434.

S3. Li WC, Zhou Q, Zhang P, Chen XW. Direct Electro Plasmonic and Optic Modulation via a Nanoscopic Electron Reservoir. Phys Rev Lett. 2022;128(21):217401.

S4. Zhou Q, Li WC, He Z, Zhang P, Chen XW. Quantum hydrodynamic model for noble metal nanoplasmonics. Phys Rev B. 2023;107(20):205413.

S5. Lin QQ, Hu S, Földes T, Huang JY, Wright D, Griffiths J, et al. Optical suppression of energy barriers in single molecule-metal binding. Sci Adv. 2022;8(25):eabp9285.

S6. Urbieta M, Barbry M, Zhang Y, Koval P, Sánchez-Portal D, Zabala N, et al. Atomic-Scale Lightning Rod Effect in Plasmonic Picocavities: A Classical View to a Quantum Effect. ACS Nano. 2018;12(1):585-95.